Power-in-bucket enhancement in tiled-aperture coherent beam combining through inducing spatial chirp

Wenhai Liang[1,2] Shuman Du,[1,2] Renjing Chen,[1,2] Chengru Wu,[1,2] Xiong Shen,[1,3]
Peng Wang,[1,3] Jun Liu,[1,2,3,*] and Ruxin Li[1,2,3]

[1]*State Key Laboratory of High Field Laser Physics and CAS Center for Excellence in Ultra-intense Laser Science,*
Shanghai Institute of Optics and Fine Mechanics, Chinese Academy of Sciences, Shanghai 201800, China

[2]*University Center of Materials Science and Optoelectronics Engineering, University of Chinese Academy of*
Sciences, Beijing 100049, China

[3]*Zhangjiang Laboratory, 100 Haike Road, Pudong, Shanghai 201210, China*

Spatial gaps between sub-beams in high-peak-power lasers with tiled-aperture-based coherent beam combining (TACBC) give rise to relatively strong sidelobes and impair the power in bucket (PIB) at far field. To address the aforementioned issue, spatial chirp is employed in this paper to fill the gaps and further enhance PIB. With two sub-beams, both simulations and experiments indicate that spatial chirp can boost PIB by 1.8 times at a gap-beam width ratio of 0.2. The same enhancement is observed in simulations even when four sub-beams are considered. To put it briefly, the spatial-chirp-assisted TACBC approach holds the potential in boosting focal intensity during constructing tens to hundreds of petawatt (PW) lasers.

I. INTRODUCTION

Laser technology is currently pursuing higher energy and shorter pulse duration to achieve ultrahigh peak power, the key to unlocking the increasingly significant applications in relativistic optics and high-field laser physics [1–5]. However, such high-peak power nearly reaches the ceiling with one single beam due to limits in manufacturing dimensions and damage thresholds of essential optics, such as nonlinear crystals and gratings.

To further improve laser peak power, Blanchot *et al.* [6] firstly proposed the TACBC scheme involving beam phasing instead of grating mosaic phasing [7,8] to obtain PW lasers in 2006. In TACBC, several small-size laser beams (or sub-beams) were coherently combined together to an ultrahigh-power integrated beam. Recently, the TACBC technology [9–13] had undergone extensive theoretical research and gained experimental success. In 2014, the TACBC of several optical parametrical amplified femtosecond beams was demonstrated together with a two-loop relative timing jitter active stabilization scheme [11]. Leshchenko *et al.* obtained relativistic intensity femtosecond laser pulses by TACBC [12]. The 1.15 PW @ 850 J laser at the Petawatt Aquitaine Laser facility (PETAL) was successfully achieved in 2017 [13]. Besides, the TACBC method was applicable when it came into the hundreds

of PW regime. The SEL facility [14] in China originally planned to reach 100 PW scale by combining four tens of PW beams. More than ten sub-beams with tens of PW were TACBC-designed to achieve 200 PW in the Exawatt Center for Extreme Light Studies [15] in Russia. Another 200 PW laser plan in Extreme Light Infrastructure [16] from Europe also adopted this multibeam combining technology.

However, there was an inevitable "gap problem" in tiled-aperture laser beam. Several theoretical [17,18] and experimental [12,19] works had shown that the spatial gaps induced relatively high sidelobes, which would weaken the main lobe of the focal spot during final focusing even under the condition of meticulous calibration and phase matching. The presence of more intense sidelobes was observed [18] when enlarging the gap of two of the same sub-beams. Then, PIB that is defined as the power ratio of the beam circled by a specific radius to the total combined output at far field decreases with the increasing the gap-beam width ratio (the ratio of gap width to beam width). Here the beam contained within a ring with a specific radius denotes the main lobe at far field. Note that only the influence of beam geometry is estimated; the wavefront error and mismatch in spectral phase are not taken into account in this paper.

Since it is the gap that hinders PIB, is it feasible to make up for the gap space between sub-beams in TACBC? In our recent works [20–22], beam smoothing by spatial chirp was proposed to decrease the beam spatial intensity

*Contact author: jliu@siom.ac.cn

modulation, aiming to increase the total input and output pulse energy in PW compressors. In this paper, we present that the gaps between sub-beams in TACBC can be filled by inducing spatial chirp to the laser beam. As a result, sidelobes at far field can be decreased, thus boosting PIB. As for TACBC with two sub-beams, simulations illustrate that the PIB enhancement ratio, defined as the PIB ratio between the conditions with and without spatial chirp, can reach 1.5 or 1.8 when gap-beam width ratio equals 0.1 or 0.2. Subsequent experiments validate these results. Four sub-beams are also analyzed to check the applicability, which realizes a PIB enhancement ratio of 1.6 or 1.8 through 200- or 290-mm spatial dispersion when gap-beam width ratio is 0.05.

II. BASELINE MODEL AND SIMULATIONS

The basic principle of PIB enhancement through spatial chirp is illustrated in Fig. 1. The normalized light field of one sub-beam right before the convergence element (lens, curved mirror and so on) can be expressed from [23] as

$$
\begin{aligned}
E_{nf_1} = \sum_i & e^{-[2\ln 2(x-\alpha_x(\omega_i-\omega_0))^2/D_{xr}^2]^m} \\
& \times e^{-[2\ln 2(y-\alpha_y(\omega_i-\omega_0))^2/D_{yr}^2]^m} \\
& \times e^{-[2\ln 2(\omega_i-\omega_0)^2/\Omega^2]^n},
\end{aligned}
$$

where α_x, α_y are the spatial chirp coefficients in X, Y directions. The amount of spatial dispersion width is $W_{SDx} = \alpha_x(\omega_s - \omega_l)/2$, $W_{SDy} = \alpha_y(\omega_s - \omega_l)/2$; ω_s, ω_l denote the frequencies of the shortest, longest wavelengths. D_{xr}, D_{yr} are the relative beam sizes in X, Y directions; ω_0 denotes the center frequency; Ω is the relative spectrum width; m and n denote the orders of super-Gaussian beam and spectrum profiles. The whole beam E_{nf} at near-field can be expressed by summing up all of the sub-beams, where other sub-beams can be written by the mathematical expression above but with some translation on the Cartesian coordinate system. In practice, spatial chirp in one direction can be ensured by the asymmetry of a four-grating compressor [24], and the other by oblique beam incidence on the diffraction gratings or by the tilted grooves [25].
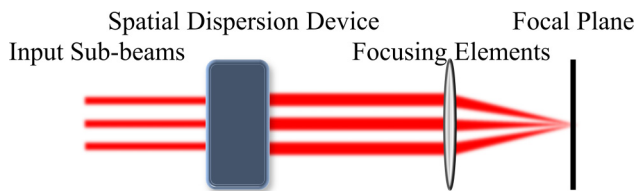

FIG. 1. The optical diagrammatic sketch of the PIB enhancement approach.

Then under the effects of focusing elements and free-space diffraction, light field can be described as the inverse Fourier transform of

$$
\mathcal{F}\left\{ E_{nf} \times \exp\left[-\frac{ik(x^2 + y^2)}{2f} \right] \right\} \times \exp\left[\frac{i(k_x^2 + k_y^2)z}{2k} \right],
$$

where the position of the convergence element is defined as $z = 0$; k denotes the wave vector and f is the focal length. Paraxial approximation is taken into consideration. When $z = f$, the output is the far-field profile.

A. Case 1, two sub-beams with a gap-beam width ratio of 0.1

The sizes of each sub-beam are set to be 180 mm in X direction and 400 mm in Y direction with gap width of 40 mm as shown in Figs. 2(a) and 2(b). Thus the combined beam width D_x equals beam height D_y with a value of 400 mm. The spectrum ranges from 825 to 1025 nm. m and n are set to be 10. Proposing that the pulses are perfectly chirp compensated, the Fourier-transform-limited (FTL) pulse duration is 14 fs.

Under the condition of no spatial chirp with zero spatial dispersion width, i.e., $\alpha_x = \alpha_y = 0$ in simulation, the far field in Figs. 2(c) and 2(d) contains a main lobe (referring to the area from the peak to positions where the intensities firstly drop to 0 or closest to 0) and a series of sidelobes, where the former one takes up 68% of the total energy.

In order to find out the exact effects of spatial chirp on beam quality, various amounts of spatial dispersion widths are induced to the input in X direction with $\alpha_x \neq 0$. Figure 3(a) shows the varying curves of PIB and peak-point power (referring to the point with maximum power) enhancement ratio with different value of W_{SDx}-D_x (the ratio between lateral spatial dispersion width and beam size). Here the parameter W_{SDx}-D_x is chosen as the independent variable rather than a sole W_{SDx} since the ratio is more comprehensive, accounting for the gap width, beam size, and induced spatial dispersion.

Obviously, PIB increases nearly linearly with W_{SDx}-D_x at first, leveling off at a value of 92% as W_{SDx}-D_x increases to 0.33 ($\alpha_x = 0.6$). Correspondingly, PIB enhancement ratio reaches 1.5. In contrast to the energy ratio, the peak-point power-enhancement ratio exhibits nearly linear growth all the time. This phenomenon is primarily attributed to the continuous increase of the input beam size in X direction as the spatial chirp increases. Consequently, the lateral size of focal spot becomes progressively smaller, and energy converges persistently in the same direction. However, an indefinite peak-point power enhancement is not the optimal outcome due to the substantial amount of spatial dispersion width required and an excessively small focus size in X direction. Hence, the situation of W_{SDx}-$D_x = 0.33$ is picked and exhibited in Figs. 2(e)–2(h). The
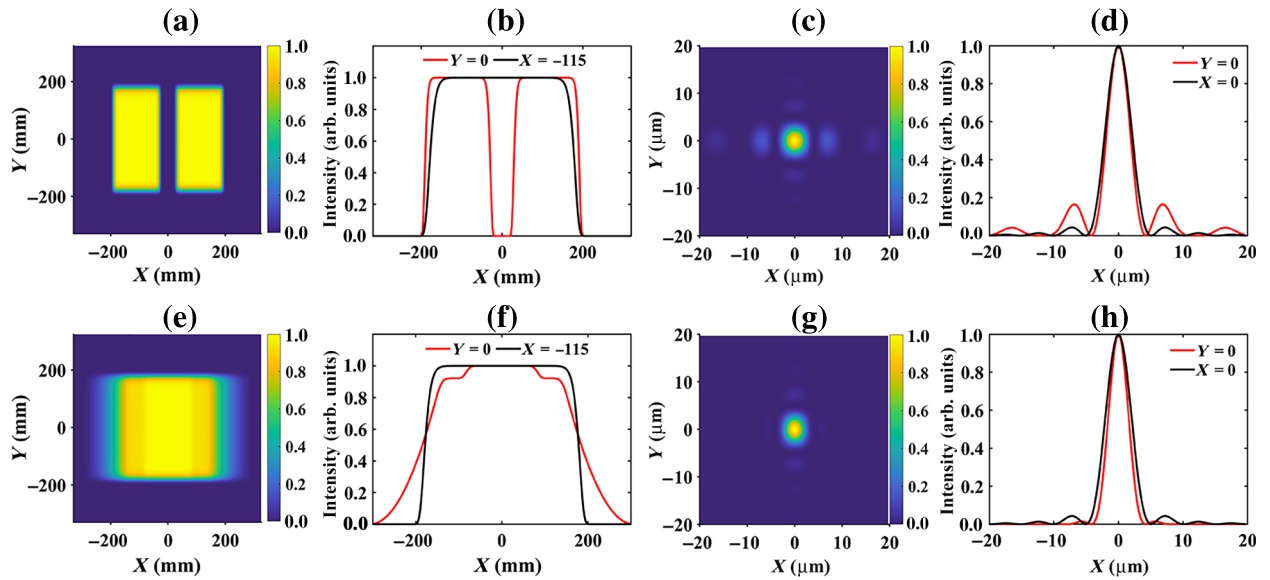
FIG. 2. (a)–(d) Beam profiles when $\alpha_x = 0$. (a) Input beam. (b) One-dimensional (1D) intensity curves of (a) at $Y = 0$ and $X = -115$ mm. (c) Beam at far field. (d) 1D intensity curves of (c) at $Y = 0$ and $X = 0$. (e)–(h) Beam profiles when $\alpha_x = 0.6$. (e) Input beam. (f) 1D intensity curves of (e) at $Y = 0$ and $X = -115$ mm. (g) Beam at far field. (h) 1D intensity curves of (g) at $Y = 0$ and $X = 0$.

gap in Fig. 2(a) is filled, which helps eliminate sidelobes at far field and enhance PIB.

B. Case 2, two sub-beams with a gap-beam width ratio of 0.2

The sizes of the sub-beam are set to be 160 mm in X direction and 400 mm in Y direction with gap width of 80 mm as shown in Fig. 4(a).

With $\alpha_x = 0$, the input beam in Fig. 4(a) has a bigger gap than beam in Fig. 2(a). As a result, the far field in Figs. 4(c) and 4(d) contains sidelobes with higher intensity, leading to a PIB of 58%.

From Fig. 3(b), PIB increases nearly linearly with W_{SDx}-D_x at first, leveling off at a value of 92% as it increases to 0.39 ($\alpha_x = 0.7$). Correspondingly, peak-point power is enhanced by 1.8 times. Similar to the last case, the growth of peak-point power-enhancement ratio remains nearly

linear all the time. Here larger spatial dispersion width is needed to reach the PIB plateau since the gap is wider. Figures 4(e)–4(h) show the beam profiles at far field when W_{SDx}-$D_x = 0.39$.

C. Case 3, four sub-beams with a gap-beam width ratio of 0.05

The sizes of one sub-beam are set to be 400 mm in X direction and 400 mm in Y direction with gap width of 40 mm as shown in Fig. 5(a).

When $\alpha_x = 0$, the input beam in Figs. 5(a) and 5(b) has gaps in both X and Y directions. As a result, the far field in Figs. 5(c) and 5(d) contains more sidelobes than the two cases above, leading to a PIB of 64%.

From Fig. 3(c), PIB increases nearly linearly with W_{SDx}-D_x at first, leveling off at a value of 95% as it increases to 0.34 ($\alpha_x = \alpha_y = 1.3$). Correspondingly,
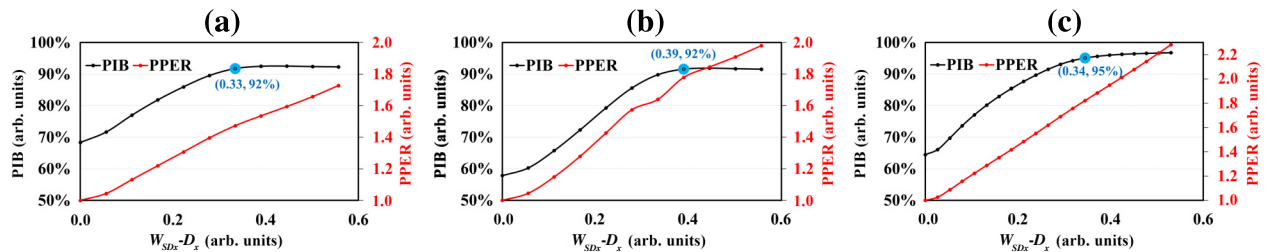

FIG. 3. Curves of PIB and peak-point power-enhancement ratio (PPER) at different W_{SDx}-D_x. (a) Two sub-beams with a gap-beam width ratio of 0.1. (b) Two sub-beams with a gap-beam width ratio of 0.2. (c) Four sub-beams with a gap-beam width ratio of 0.05.
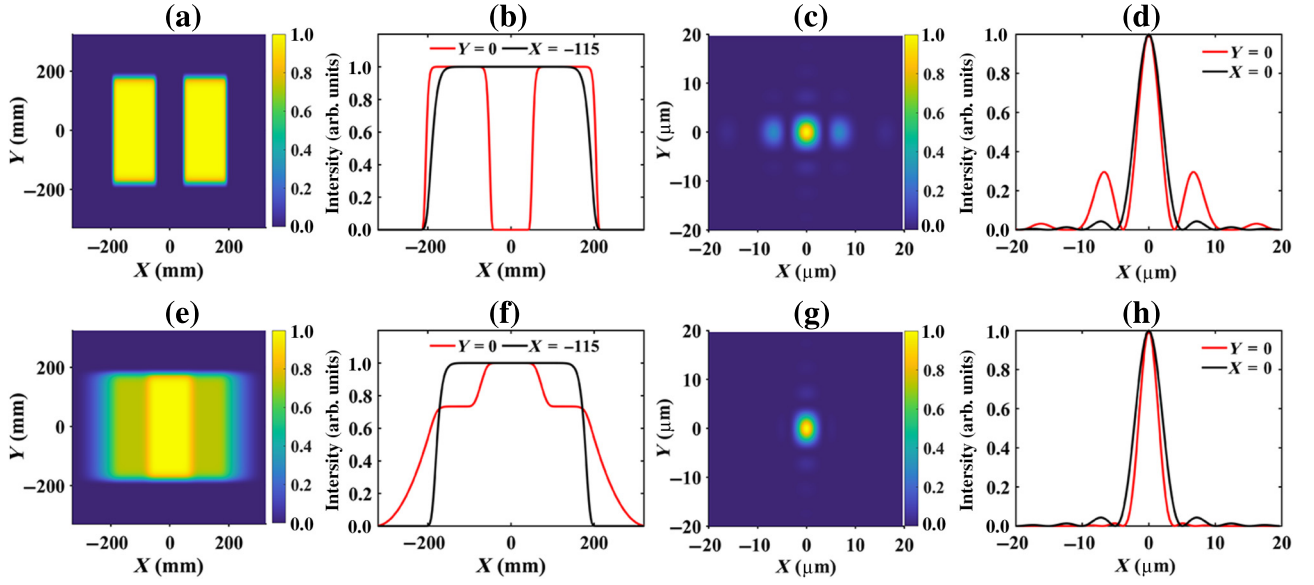
FIG. 4. (a)–(d) Beam profiles when $\alpha_x = 0$. (a) Input beam. (b) 1D intensity curves of (a) at $Y = 0$ and $X = -115$ mm. (c) Beam at far field. (d) 1D intensity curves of (c) at $Y = 0$ and $X = 0$. (e)–(h) Beam profiles when $\alpha_x = 0.7$. (e) Input beam. (f) 1D intensity curves of (e) at $Y = 0$ and $X = -115$ mm. (g) Beam at far field. (h) 1D intensity curves of (g) at $Y = 0$ and $X = 0$.

peak-point power is enhanced by 1.8 times. Similar to the two cases above, the growth of peak-point power-enhancement ratio remains nearly linear all the time.

Here, the situation of W_{SDx}-$D_x = 0.24$ ($\alpha_x = \alpha_y = 0.9$) with peak-point power-enhancement ratio of 1.6 is picked and exhibited in Figs. 5(e)–5(h) due to the ease of inducing less spatial dispersion width.

III. EXPERIMENT AND RESULTS

Based on a 1-kHz Ti:sapphire laser system with output pulse energy of 6 mJ and uncompressed pulse, the proof-of-principle experimental setup is shown in Fig. 6.

Firstly, a $4f$ system ($4f_1$) consisting of $L1$ ($f_1 = -200$ mm) and $L2$ ($f_2 = 1500$ mm) is used to expand the beam. Then a circular soft-edge aperture with a diameter
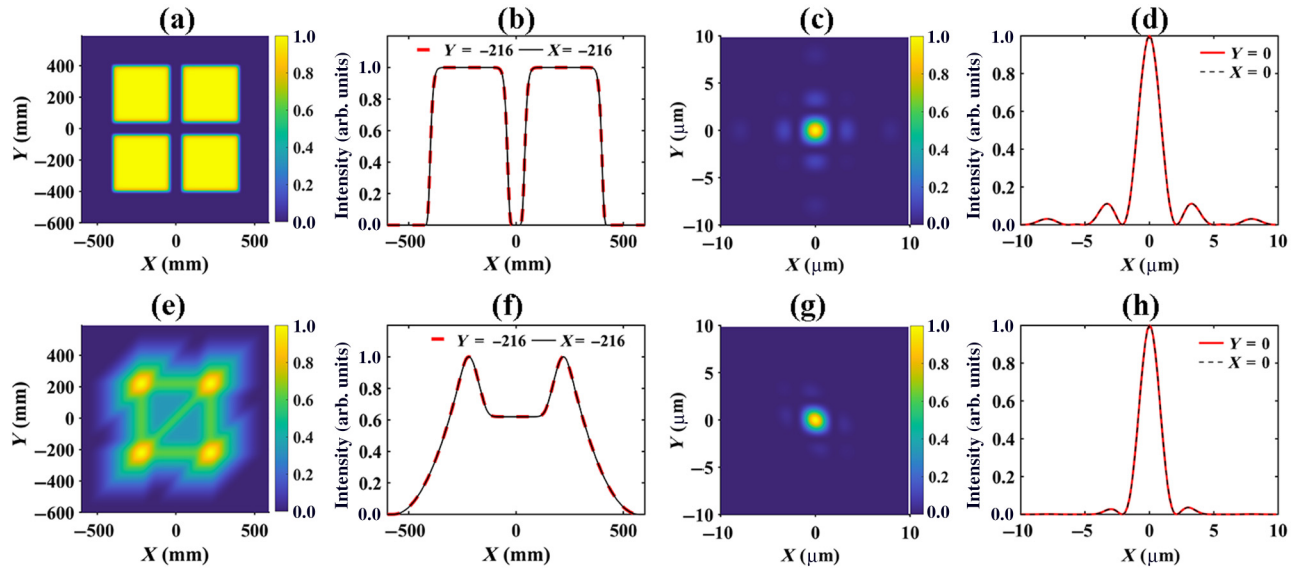

FIG. 5. (a)–(d) Beam profiles when $\alpha_x = \alpha_y = 0$. (a) Input beam. (b) 1D intensity curves of (a) at $Y = -216$ mm and $X = -216$ mm. (c) Beam at far field. (d) 1D intensity curves of (c) at $Y = 0$ and $X = 0$. (e)–(h) Beam profiles when $\alpha_x = \alpha_y = 0.9$. (e) Input beam. (f) 1D intensity curves of (e) at $Y = -216$ mm and $X = -216$ mm. (g) Beam at far field. (h) 1D intensity curves of (g) at $Y = 0$ and $X = 0$.
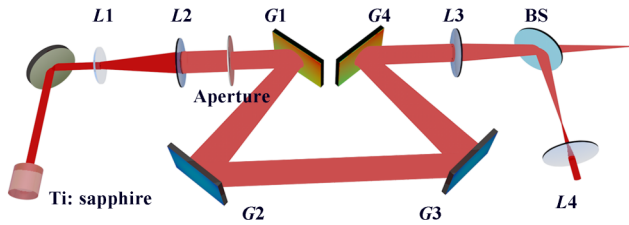
FIG. 6. The optical setup. $L1$ is a plano-concave lens. $L2$–$L4$ are plano-convex lenses. $G1$–$G4$ are gratings with groove density of 1480 lines/mm. BS, beam splitter.

of about 18 mm intercepts the beam center with pulse energy of 1.2 mJ for the consideration of beam homogeneity before the beam is sent into the grating compressor. The compressed pulses are converged by $L3$ ($f_3 = 1500$ mm) to obtain the focus. A beam splitter with a 50:50 reflection-to-transmission ratio is located behind $L3$ and far away from the focus to reflect partial light to $L4$ ($f_4 = 250$ mm), which forms another $4f$ configuration ($4f_2$) together with $L3$, to attain the collimated and size-reduced beam for near-field characterization. Here the focus is captured by a charge-coupled device (CCD, BC106, Thorlabs). Besides, the pulse energy is measured to be 380 µJ transmitted through the beam splitter due to the energy loss caused by mirror and grating reflections and high-order grating diffractions. $L3$ is placed 1500 mm behind $G4$, while another CCD is placed at the rear focal plane of $L4$, so as to capture the

beam image right after $G4$ and keep free-space diffraction from the near-field beam.

In this paper, spatial chirp is induced through transforming a four-grating compressor (FGC) into an asymmetric four-grating compressor (AFGC). There are also other methods such as prisms that can serve as spatial chirp introducers. According to former researches [20,21,24,26], the transition just requires simple translation of two gratings, such as $G2$ and G3 in Fig. 6. Denoting the perpendicular distance between the grating pairs ($G1$ and $G2$, $G3$ and $G4$) as $L1$ and $L2$, the compressor is classified as AFGC when $L1 \neq L2$. As long as the value of $L1 + L2$ remains constant, the induced spectral dispersion provided by the compressor remains the same. The induced spatial dispersion width W_{SD} of the compressor can be expressed according to [24] as follows:

$$W_{SD} = (\tan \beta_{\lambda_l} - \tan \beta_{\lambda_s}) \times \cos \alpha \times (L2 - L1),$$

where β_{λ_s} and β_{λ_l} are the diffraction angles of the shortest and longest wavelengths of the input laser. α denotes the incident angle to $G1$, which is 51° in this context. The induced spatial dispersion width is linearly related to the difference between $L1$ and $L2$. Three cases of compressor configurations with $L1 - L2 = 0$, 60, and 120 mm are investigated, corresponding to spatial dispersion width of 0, 6.5, and 13 mm.

Figure 7 displays the near-field beams (a)–(c) and foci (d)–(f) when the gap width equals 0. Under such circumstances, the energy is essentially concentrated in the main
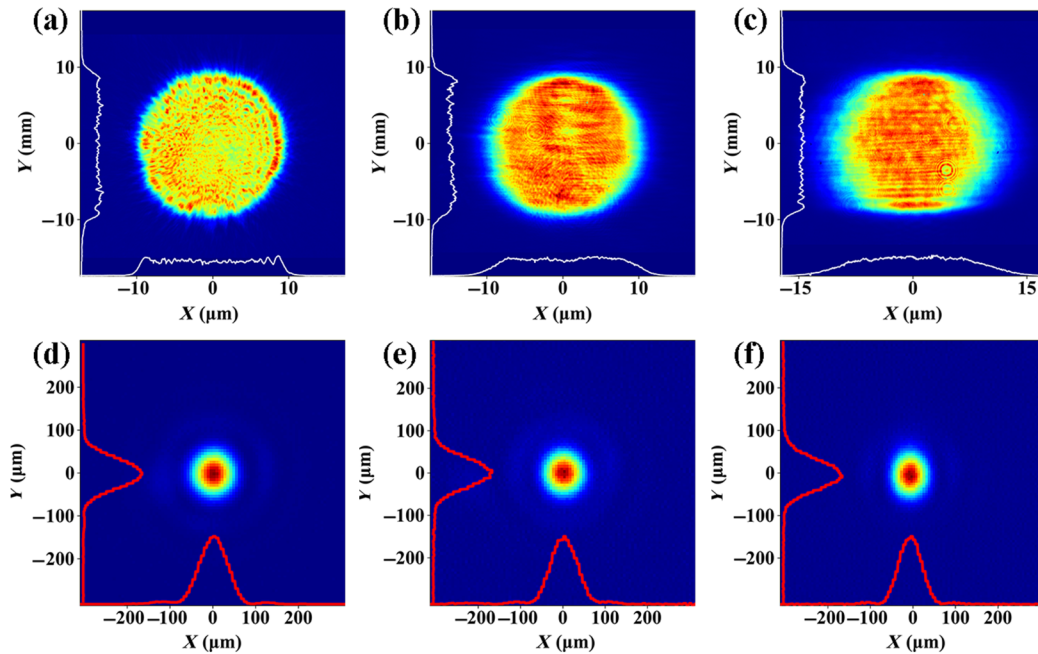

FIG. 7. (a)–(c) Near-field beams of $W_{SD} = 0, 6.5$ and 13 mm. The normalized 1D intensity curves at $Y = 0$ and $X = 0$ are plotted in white. (d)–(f) Far-field beams corresponding to the three cases above. The normalized 1D intensity curves at $Y = 0$ and $X = 0$ are plotted in red.

FIG. 8. (a)–(c) Near-field beams of $W_{SD} = 0, 6.5$ and 13 mm. The normalized 1D intensity curves at $Y = 0$ and $X = 0$ are plotted in white. (d)–(f) Far-field beams corresponding to the three cases above. The normalized 1D intensity curves at $Y = 0$ and $X = 0$ are plotted in red.
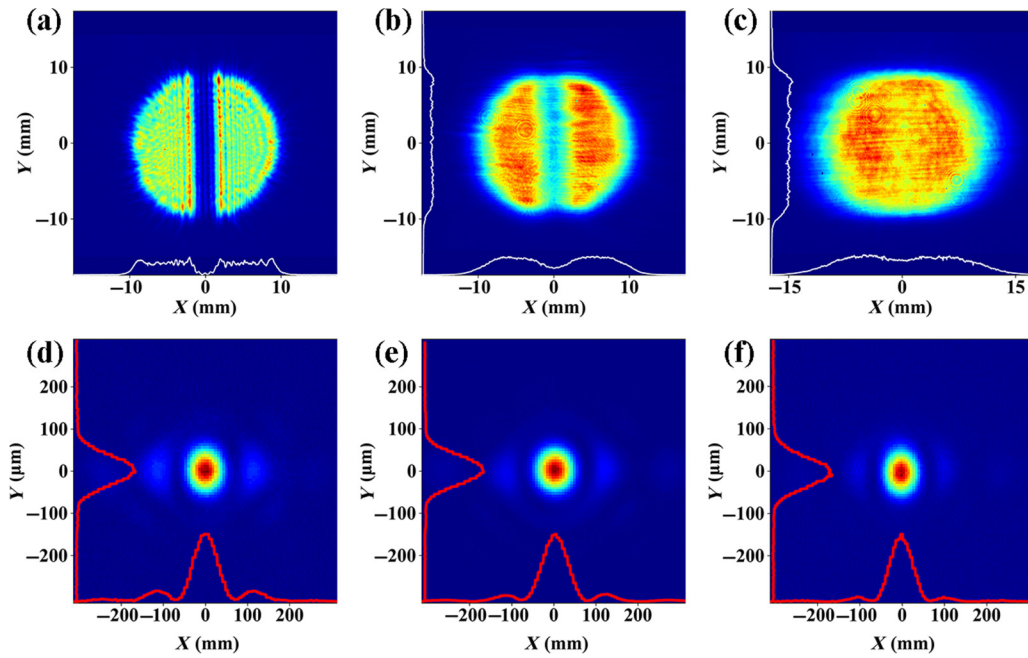
lobe and there are no discernible sidelobes at the foci. Furthermore, the addition of lateral spatial dispersion width causes an expansion to the lateral size of the near-field beam, which in turn decreases the lateral size of the focus. The PIB and peak-point power-enhancement ratio—two metrics that assess the quality of the focal spots—are computed utilizing the one-dimensional intensity profile along the X axis rather than scanning the whole image as in the simulation in an effort to minimize environmental white noise. The PIBs for (d), (e), and (f) in Fig. 7 are 94%, 93%, 94%, respectively.

A 3-mm-wide soft-edged paper strip is positioned in front of G1 subsequently to block the central portion of the light beam vertically, which can be treated as two sub-beams with gap and a gap-beam width ratio of 0.17. The captured spatial profiles are illustrated in Fig. 8. As the modeling indicated, the gap is successfully filled with spatial dispersion, and the main lobe energy of focus experiences a greater concentration. Specifically, the PIBs are 70%, 81% and 89% in Figs. 8(d)–8(f), respectively, while the peak-point power-enhancement ratios of (e) and (f) reach 1.5 and 1.8 in comparison to (d).

The nature of intensity change in the gap region with the introduction of spatial chirp is the shift of spectral components. Spatial chirp effect allows light from a shorter wavelength band on one sub-beam and a longer one from the other sub-beam to fill the gap between the two sub-beams. The output laser is directly injected into a fiber connected with a spectrometer (USB4000, Ocean Optics)

and the spectra at the beam center are recorded in Fig. 9. The spectral profile in an FGC at $W_{SD} = 0$ primarily arises from scattering and subtle edge diffraction effects, which is very weak. When $W_{SD} = 6.5$ mm, the spectrum consists of two peaks at both longer wavelengths and shorter wavelengths. Meanwhile, it is evident that there is still a noticeable gap in Fig. 8(b). When $W_{SD} = 13$ mm, the spectrum profile is filled with entire wavelength components with relatively strong intensities.

Another soft-edged paper strip with larger width of 3.8 mm, which corresponds to the gap-beam width ratio of 0.21, is used to cause more serious sidelobes in Fig. 10. The PIBs are 58%, 73% and 85% corresponding to Figs. 10(d)–10(f), respectively, where the peak-point
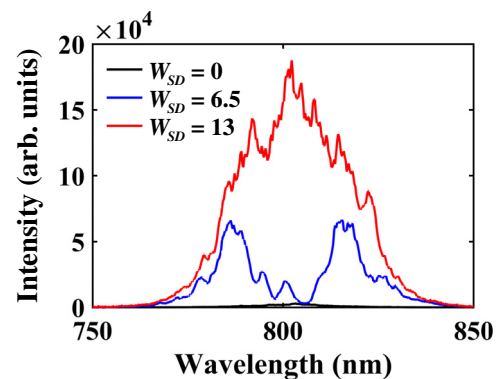

FIG. 9. Spectra at the output beam center.

power of (e) and (f) is improved by a factor of 1.4 and 1.7 compared to (d).

Based on the experimental results above, several conclusions can be drawn. Firstly, the proposed spatial chirp method has a significant effect on improving the intensity and quality of the focal spot. Secondly, as the gap-beam width ratio increases, the number and intensity of sidelobes also increase. Under such a condition and the same amount of induced spatial dispersion width, the peak-point power-enhancement ratio and the proportion of main lobe energy is smaller. In other words, with a larger gap-beam width ratio, larger spatial dispersion width is required to achieve an equivalent PIB. Thirdly, the spatial chirp approach significantly improves the focal spot for TACBC with different gap-beam width ratios, emphasizing its universality. Fourthly, with the introduction of spatial chirp, the PIB does not show a linear growth trend, mainly because it tends towards saturation and is affected by environmental noise. Lastly, with the introduction of spatial chirp, peak-point power-enhancement ratio will not continue to grow indefinitely, mainly due to white noise and limitations imposed by the face flaws of the focusing element, making it impossible for the focus size to shrink indefinitely. The experimental results are consistent with the simulations.

Besides energy, the pulse duration is also one of the key parameters for ultrahigh-power laser. During the transformation from FGC to AFGC, an indispensable step is to testify that the compressor is well aligned. Hence the whole output beam is injected into a home-made self-referenced spectral interferometer setup to characterize the temporal properties, which are shown in Fig. 11.

Here, two scenarios are presented, namely FGC in Figs. 11(a)–11(c) and AFGC with a spatial dispersion width of 13 mm in Figs. 11(d)–11(f). In Fig. 11(c), the measured temporal profile closely resembles the one of FTL, indicating that the FGC is well aligned. Essentially, the pulse widths of the FGC and AFGC are consistent, with values of 39.6 and 40.7 fs. The slight spectral profile differences between AFGC and FGC shown in Figs. 11(a) and 11(d) are primarily caused by the spectral component shift on beam cross section resulted from spatial chirp. However, the differences are so minimal as to barely impact the pulse width and subsequent beams. Former researches [21,23] also indicate that the spatial chirp scarcely influence the temporal width at far field due to the spatiotemporal focusing effect.

IV. DISCUSSIONS

Considering a very specific application, the synthetic aperture compression scheme PETAL [9,27] serves as an illustrative example. The sub-beam sizes are 170×85 mm^2, assuming a super-Gaussian spectrum ranging from 1045 to 1061 nm.

When gap-beam width ratio is set to be 0.1, which corresponds to a gap width of 19 mm, the simulation results are shown below. Without spatial chirp, the gap at
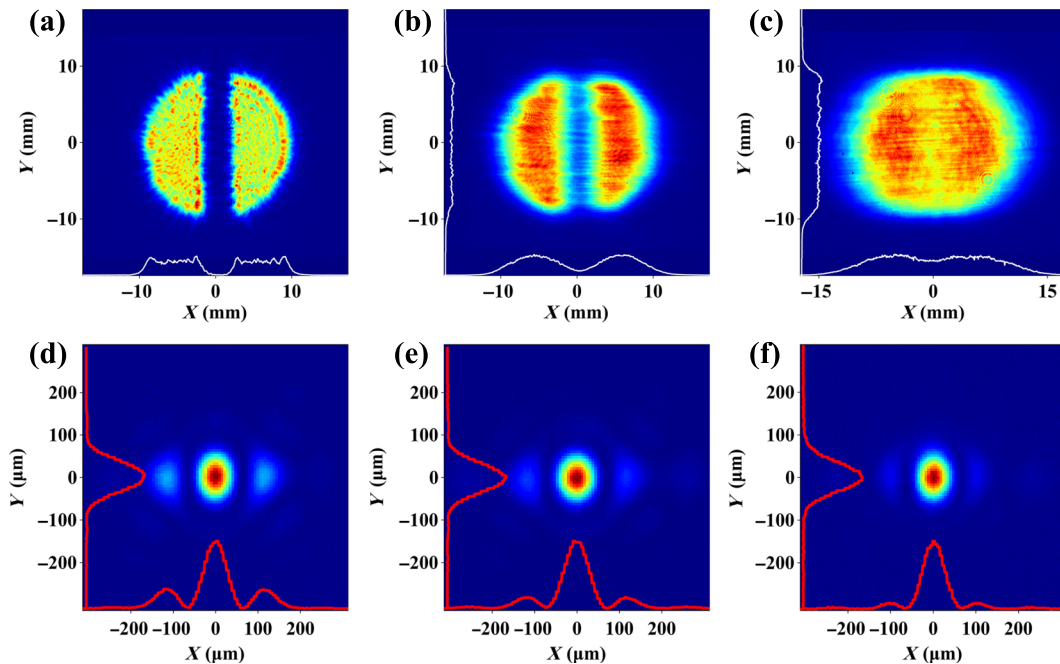

FIG. 10. (a)–(c) Near-field beams of $W_{SD} = 0, 6.5$ and 13 mm. The normalized 1D intensity curves at $Y = 0$ and $X = 0$ are plotted in white. (d)–(f) Far-field beams corresponding to the three cases above. The normalized 1D intensity curves at $Y = 0$ and $X = 0$ are plotted in red.
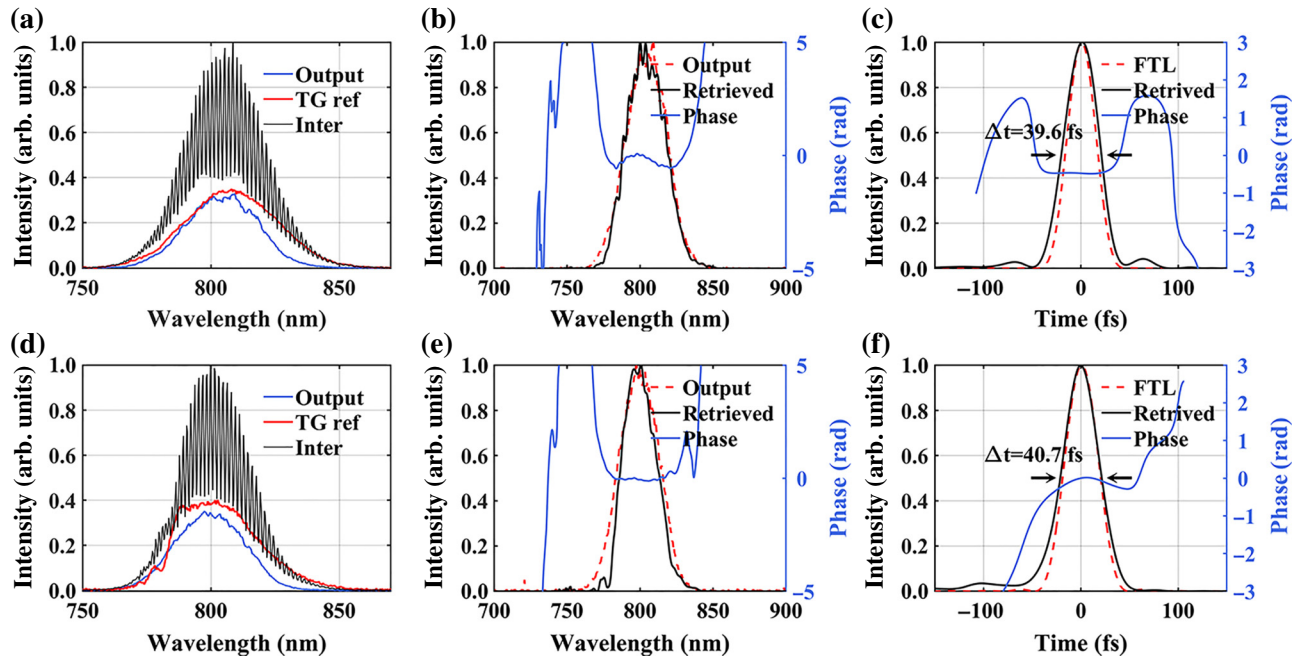
FIG. 11. (a) Spectral intensity profiles of FGC (blue), the transient grating (TG) reference spectrum (red), and interference between them (black). (b) Measured spectrum of FGC (red), retrieved spectrum (black) and retrieved phase (blue). (c) Retrieved temporal profile of FGC (black), FTL pulse (red) and retrieved phase (blue). (d)–(f) Corresponding curves of (a)–(c) but for AFGC.

near-field beam leads to a series of sidelobes at far field, and the main lobe energy takes up 70% of the total energy. Next, if $\alpha_x = 2$ and spatial dispersion width along X direction is 27.2 mm, the gap between the two sub-beams is filled, as Fig. 12(e) shows. And the main lobe energy of focus increases to 91%.

The PETAL and the first simulation case in Sec. II have the same gap-beam width ratio of 0.1, while the spatial chirp coefficients vary significantly (2 versus 0.6) to attain a comparable main lobe energy ratio (91% versus 92%). This phenomenon is primarily due to the relatively narrow spectral range of the PETAL case.
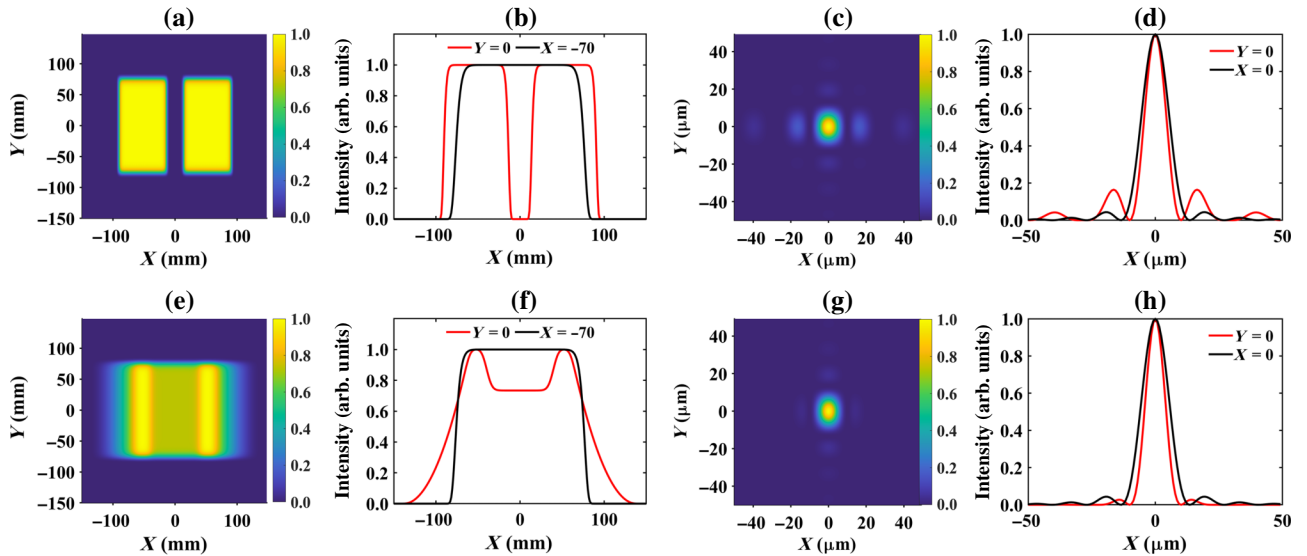

FIG. 12. (a)–(d) Beam profiles when $\alpha_x = 0$. (a) Input beam. (b) 1D intensity curves of (a) at $Y = 0$ and $X = -70$ mm. (c) Beam at far field. (d) 1D intensity curves of (c) at $Y = 0$ and $X = 0$. (e)–(h) Beam profiles when $\alpha_x = 2$. (e) Input beam. (f) 1D intensity curves of (e) at $Y = 0$ and $X = -70$ mm. (g) Beam at far field. (h) 1D intensity curves of (g) at $Y = 0$ and $X = 0$.

As the peak power increases, nonlinear effects may affect the gap-filling process, as exemplified by lenses $L2$ and $L3$ below.

Lenses $L2$ and $L3$ are both made of BK7 glass with thickness of about 8 mm. According to the B-integral formula below:

$$B = \frac{2\pi}{\lambda} \int n_2 I(z) dz$$

in which λ is 800 nm, denoting the central wavelength; $I(z)$ is the intensity of light along the optical axis z, and $n_2 = 3.3 \times 10^{-20}$ m^2/W, is the nonlinear refraction coefficient.

The beam within $L2$ owns a beam radius of 37.5 mm, pulse energy of about 6 mJ. Note that the laser pulse at L2 is uncompressed and has a pulse width on the order of nanosecond to picosecond, making the B integral induced by $L2$ trivial.

The beam within $L3$ owns a beam radius of 9 mm, pulse energy of about 0.8 mJ, resulting in a B integral of 0.16. If the pulse energy exceeds 5 mJ at $L3$, corresponding to a B integral of 1 and intensity of 5×10^{14} W/m^2, it is necessary to take into account the effect of nonlinear effects such as self-phase modulation on the coherent beam combining. However, in ultrahigh-power laser systems, the focusing elements after the compressor are generally reflective optics, such as off-axis parabolic mirrors, in which case the pulse energy is not limited by the lens-induced nonlinearity considered here.

All in all, the nonlinearity caused by $L2$ can be neglected, partly because the considerable pulse width in front of the compressor, and partly because the beam-expansion stage consists of $L1$ and $L2$ is unnecessary in application. As for $L3$, it set limits to the pulse energy and intensity in this case. Yet, $L3$ can be avoided in application, hence leaving the pulse energy unconstrained by the lens-induced nonlinearity.

V. CONCLUSIONS

In summary, to conquer the low PIB problem induced by spatial gaps between sub-beams of TACBC configurations, the spatial chirp approach is proposed in this paper. In both simulation and experiment settings, it has been verified that PIB can be boosted by more than 1.5–1.8 times, which specifically depends on the gap-beam width ratio and amount of spatial dispersion. The enhancement occurs without apparent energy loss or pulse-duration changes, implying a potential increase of over 1.5 times in the practical focal intensity of the combined laser. Simultaneously, spatial chirp helps smooth the near-field beam profile, reducing the laser spatial intensity modulation. Moreover, these results demonstrate versatility across various sub-beam quantities and gap widths. Thus, this method represents a pivotal step in advancing focal intensity, opening avenues for the reliable and efficient construction of ultrahigh-peak-power lasers with TACBC technology.

Data underlying the results presented in this paper are not publicly available at this time but may be obtained from the authors upon reasonable request.

[1] M. M. Günther, O. N. Rosmej, P. Tavana, M. Gyrdymov, A. Skobliakov, A. Kantsyrev, S. Zähter, N. G. Borisenko, A. Pukhov, and N. E. Andreev, Forward-looking insights in laser-generated ultra-intense γ-ray and neutron sources for nuclear application and science, Nat. Commun. **13**, 170 (2022).

[2] J. W. Yoon, Y. G. Kim, I. W. Choi, J. H. Sung, H. W. Lee, S. K. Lee, and C. H. Nam, Realization of laser intensity over 10^{23} W/cm^2, Optica **8**, 630 (2021).

[3] L. Fedeli, A. Sainte-Marie, N. Zaim, M. Thévenet, J. L. Vay, A. Myers, F. Quéré, and H. Vincenti, Probing strong-field QED with Doppler-boosted petawatt-class lasers, Phys. Rev. Lett. **127**, 114801 (2021).

[4] T. Liu, K. Zhang, Z. Qi, S. Chen, C. Feng, H. Deng, B. Liu, and D. Wang, Matching-based two-color x-ray free-electron laser generation utilizing laser–plasma accelerated electron beam, High Power Laser Sci. Eng. **10**, e1 (2022).

[5] H. H. An, *et al.*, Accelerated protons with energies up to 70 MeV based on the optimized SG-II peta-watt laser facility, High Power Laser Sci. Eng. **11**, e63 (2023).

[6] N. Blanchot, G. Marre, J. Néauport, E. Sibé, C. Rouyer, S. Montant, A. Cotel, C. Le Blanc, and C. Sauteret, Synthetic aperture compression scheme for a multipetawatt high-energy laser, Appl. Opt. **45**, 6013 (2006).

[7] J. Qiao, A. Kalb, T. Nguyen, J. Bunkenburg, D. Canning, and J. H. Kelly, Demonstration of large-aperture tiled-grating compressors for high-energy, petawatt-class, chirped-pulse amplification systems, Opt. Lett. **33**, 1684 (2008).

[8] Z. Li, S. Li, C. Wang, Y. Xu, F. Wu, Y. Li, and Y. Leng, Stable and near Fourier-transform-limit 30 fs pulse compression with a tiled grating compressor scheme, Opt. Express **23**, 33386 (2015).

[9] N. Blanchot, *et al.*, Overview of PETAL, the multi-petawatt project on the LIL facility, Plasma Phys. Controlled Fusion **50**, 124045 (2008).

[10] K. Liu, L. Song, Y. Liu, X. Wang, Z. Huang, Y. Tang, X. Wang, Z. Liu, and Y. Leng, Simultaneous measurement of the absolute and relative time delay of a tiled-aperture coherent beam combination via the double-humped spectral beam interferometry, Opt. Express **28,** 35498 (2020).

[11] S. N. Bagayev, V. I. Trunov, E. V. Pestryakov, S. A. Frolov, V. E. Leshchenko, A. E. Kokh, and V. A. Vasiliev, Super-intense femtosecond multichannel laser system with coherent beam combining, Laser Phys. **24,** 074016 (2014).

[12] V. E. Leshchenko, V. A. Vasiliev, N. L. Kvashnin, and E. V. Pestryakov, Coherent combining of relativistic-intensity femtosecond laser pulses, Appl. Phys. B **118,** 511 (2015).

[13] N. Blanchot, *et al.*, 1.15 PW–850 J compressed beam demonstration using the PETAL facility, Opt. Express **25,** 16957 (2017).

[14] E. Cartlidge, The light fantastic, Science **359,** 382 (2018).

[15] A. Shaykin, I. Kostyukov, A. Sergeev, and E. Khazanov, Prospects of PEARL 10 and XCELS Laser Facilities, Reza Kenkyu **42,** 141 (2014).

[16] J. P. Chambaret, *et al.*, in *Proc. SPIE* (2010), pp. 77211D.

[17] D. Wang and Y. Leng, A method for aligning a femtosecond multi-petawatt coherent beam combining system, Appl. Phys. B **127,** 41 (2021).

[18] D. Wang and Y. Leng, Simulating a four-channel coherent beam combination system for femtosecond multi-petawatt lasers, Opt. Express **27,** 36137 (2019).

[19] C. Peng, X. Li, X. Liang, and R. Li, Four-beam tiled-aperture coherent beam combining of high-power fem-

[20] tosecond laser with two compressors, IEEE Photonics J. **14,** 1 (2022).

[20] S. Du, X. Shen, W. Liang, P. Wang, J. Liu, and R. Li, A 100-PW compressor based on single-pass single-grating pair, High Power Laser Sci. Eng. **11,** e4 (2023).

[21] X. Shen, S. Du, W. Liang, P. Wang, J. Liu, and R. Li, Two-step pulse compressor based on asymmetric four-grating compressor for femtosecond petawatt lasers, Appl. Phys. B **128,** 159 (2022).

[22] J. Liu, X. Shen, S. Du, and R. Li, Multistep pulse compressor for 10 s to 100 s PW lasers, Opt. Express **29,** 17140 (2021).

[23] G. Zhu, J. v. Howe, M. Durst, W. Zipfel, and C. Xu, Simultaneous spatial and temporal focusing of femtosecond pulses, Opt. Express **13,** 2153 (2005).

[24] W. Liang, S. Du, R. Chen, X. Wang, X. Liu, X. Chen, X. Shen, J. Liu, and R. Li, Viability verification of asymmetric four-grating compressor in SEL-100 PW frontend, Opt. Commun. **557,** 130317 (2024).

[25] E. Khazanov, 2D-smoothing of laser beam fluctuations in optical compressor, Laser Phys. Lett. **20,** 125001 (2023).

[26] X. Yang, X. Tang, Y. Liu, J. Bin, and Y. Leng, Beam smoothing by introducing spatial dispersion for high-peak-power laser pulse compression, Opt. Express **31,** 33753 (2023).

[27] N. Blanchot, *et al.*, Experimental demonstration of a synthetic aperture compression scheme for multi-petawatt high-energy lasers, Opt. Express **18,** 10088 (2010).